Seasonal variations of the mesospheric Fe layer at Rothera, Antarctica (67.5°S, 68.0°W)

Chester S. Gardner,[1] Xinzhao Chu,[2] Patrick J. Espy,[3] John M. C. Plane,[4] Daniel R. Marsh,[5] and Diego Janches[6]

Received 21 June 2010; revised 26 October 2010; accepted 3 November 2010; published 22 January 2011.

[1] Lidar observations of Fe densities between 75 and 105 km above Rothera, Antarctica, are used to characterize the seasonal variations of the mesospheric Fe layer near the Antarctic Circle and the differences are compared to the South Pole. The maximum Fe abundance occurs in late autumn (early May) at Rothera, rather than in midwinter. A secondary Fe enhancement occurs 6 months later in late spring (October–November) prior to the formation of polar mesospheric cloud (PMC) layers in summer. The midsummer Fe layer is 3 km lower at Rothera because Fe depletion by PMC layers near the mesopause is not as extensive or as complete as at the South Pole. These observations are modeled satisfactorily using a mesospheric one-dimensional Fe chemistry model driven by a general circulation model and including a detailed micrometeoroid flux and ablation model. Our study shows that the autumnal maximum in the Fe abundance is caused primarily by the seasonal temperature maximum in the mesopause region, reinforced by the seasonal peak in the meteor input function (MIF). The Fe abundance at Rothera declines throughout the winter in response to the decrease in the MIF and the slowly falling temperatures. The modeled Fe injection rate is ~5 times smaller while the eddy diffusivity values between 80 and 90 km are 4.1 times smaller than the corresponding values used in the South Pole model. This comparison demonstrates the sensitivity of the metal atom densities to the balance between injection by meteoric ablation and removal by downward transport.

Citation: Gardner, C. S., X. Chu, P. J. Espy, J. M. C. Plane, D. R. Marsh, and D. Janches (2011), Seasonal variations of the mesospheric Fe layer at Rothera, Antarctica (67.5°S, 68.0°W), *J. Geophys. Res.*, *116*, D02304, doi:10.1029/2010JD014655.

1. Introduction

[2] Meteoric ablation is the source of metal atom layers in the mesosphere and lower thermosphere (MLT) between about 75 and 110 km altitude [e.g., *Plane*, 1991, 2003; *Kane and Gardner*, 1993a; *von Zahn et al.*, 2002]. Their existence was discovered by analyzing the spectra of atmospheric nightglow emissions [*Slipher*, 1929; *Hunten*, 1967] and later confirmed by resonance fluorescence lidar measurements [e.g., *Bowman et al.*, 1969; *Felix et al.*, 1973; *Granier et al.*, 1985, 1989]. During the past four decades lidar techniques have been developed to measure mesospheric Na, Fe, K, Ca, Ca^+, and Li. Nowadays narrowband Fe, Na, and K lidars are used routinely to measure temperature and wind profiles in these metal layers, enabling detailed studies of the thermal structure, dynamics, and chemistry of the mesopause region (see summary by *Chu and Papen* [2005]).

[3] *Granier et al.* [1989] made the first lidar measurements of the Fe layer at Haute Provence, France (40°N). These were followed by more extensive observations of the seasonal variations of mesospheric Fe by *Kane and Gardner* [1993b] at Urbana, Illinois (40°N), *Raizada and Tepley* [2003] at Arecibo, Puerto Rico (18°N), *Gardner et al.* [2005] at the South Pole (90°S), and *Yi et al.* [2009] at Wuhan, China (30°N). Less extensive high-latitude measurements in the Northern Hemisphere have been reported by *Alpers et al.* [1990] at Andoya, Norway (69°N), *Gerding et al.* [2000] at Kühlungsborn, Germany (54°N), and *Gardner et al.* [2001] at the North Pole (90°N). These observations have revealed large seasonal and latitudinal variations of Fe densities that are quite different than those of Na, K, and Ca [e.g., *Plane*, 1991, 2003; *Yi et al.*, 2009].

[4] Laboratory studies of the relevant Fe chemical reactions, coupled with atmospheric modeling, have complemented observations by providing a deeper understanding of the observed Fe layer features and their relationships to the

[1]Department of Electrical and Computer Engineering, University of Illinois at Urbana-Champaign, Urbana, Illinois, USA.
[2]Cooperative Institute for Research in Environmental Sciences and Department of Aerospace Engineering Sciences, University of Colorado at Boulder, Boulder, Colorado, USA.
[3]Department of Physics, Norwegian University of Science and Technology, Trondheim, Norway.
[4]School of Chemistry, University of Leeds, Leeds, UK.
[5]National Center for Atmospheric Research, Boulder, Colorado, USA.
[6]Colorado Research Associates, Northwest Research Associates Inc., Boulder, Colorado, USA.

0148-0227/11/2010JD014655

Table 1. Lidar Observations of Mesospheric Fe at Rothera, 2002–2005

	Jan	Feb	Mar	Apr	May	Jun	Jul	Aug	Sep	Oct	Nov	Dec	Total
Days	10	3	4	5	7	9	8	2	2	2	4	13	69
Hours	139.5	17	24.5	29	45.5	68	45.5	10.5	10.5	9	14	132	545

meteor input function (MIF) and to MLT composition and dynamics [*Helmer et al.*, 1998; *Plane et al.*, 1999, 2003; *Plane*, 2003; *Vondrak et al.*, 2006; *Woodcock et al.*, 2006; *Saunders and Plane*, 2006; *Zhou et al.*, 2008]. Above about 95 km ion chemistry predominates where ablated Fe atoms are converted to Fe^+ by charge transfer with ambient NO^+ and O_2^+ ions. The removal of Fe on the underside of the layer below 85 km involves the formation of the relatively stable reservoir FeOH through a series of reactions beginning with the oxidation of Fe by O_3. However, FeOH is recycled back to Fe by reaction with H; this reaction has a significant activation energy which causes the partitioning of iron between Fe and FeOH to shift to the former at higher temperatures. FeOH (and other Fe-containing molecules) are then permanently removed by forming or condensing onto meteoric smoke particles [*Saunders and Plane*, 2006]. The meteoric influx of Fe is balanced by its downward transport to the chemical sinks below 85 km by a variety of mechanisms including molecular diffusion, turbulent mixing, and nonbreaking gravity waves [*Gardner and Liu*, 2010]. The residence time for a typical Fe atom in the layer, before it is removed in a stable reservoir, is several days.

[5] Observations by the University of Illinois group at the South Pole have revealed additional interactions that contribute significantly to Fe and Na layer morphology at extreme high latitudes. During summer, polar mesospheric clouds (PMCs) form between 80 and 90 km near the cold summer mesopause. These nanometer-scale water ice particles can heterogeneously remove metal atoms from the atmosphere in their vicinity. In fact, laboratory studies, modeling, and lidar measurements have confirmed that PMCs substantially deplete Fe and Na inside PMC layers at the South Pole during the summer season [*Plane et al.*, 2004; *Gardner et al.*, 2005]. Consequently, PMCs have a significant impact on Fe and Na layer abundances, heights, and widths. In addition, it was found that the wintertime convergence of the meridional flux of Fe and Na over the South Pole plays a crucial role in maintaining the abundances of the metal layers at this site. Modeling shows that during the winter, meridional flux convergence contributes nearly as much atomic Fe and Na (~70%) to the mesopause region above the pole as meteoric ablation [*Gardner et al.*, 2005].

[6] In this paper we report the seasonal variations of the Fe layer above the British Antarctic Survey research station at Rothera, Antarctica (67.5°S, 68.0°W). The observations were conducted from December 2002 to March 2005 using the Fe Boltzmann lidar that was previously deployed at the South Pole. Rothera is located near the Antarctic Circle on Adelaide Island along the west coast of the Antarctic Peninsula. PMCs form in the summer mesopause region above Rothera; however, the clouds are less prevalent, not as bright, and they occur at lower altitudes than at the South Pole because the MLT temperatures are warmer [*Chu et al.*, 2003, 2004, 2006]. Rothera is far enough from the pole that horizontal convergence of the metal atom fluxes is negligible. In addition, stratospheric gravity wave activity in winter is significantly more intense above Rothera than at the South Pole [*Yamashita et al.*, 2009], which probably enhances the downward vertical transport of MLT constituents by turbulent mixing and gravity waves. Therefore, it is not surprising that the seasonal structure of the Fe layer is considerably different from that observed at the South Pole. We focus on three key differences: (1) the maximum Fe abundance, which occurs in late autumn rather than midwinter and is related to the mesopause region temperature and MIF maxima; (2) the decrease of Fe abundance throughout the winter, which is related to decreasing temperatures and MIF and perhaps to enhanced vertical constituent transport associated with gravity waves; and (3) the summer Fe layer height, which is 3 km lower at Rothera and is related to Fe depletion by PMCs. The observations are compared to mesospheric Fe chemistry and meteor flux models developed by Plane, Janches, and coworkers [*Plane et al.*, 2003, 2004; *Janches et al.*, 2006; *Vondrak et al.*, 2008; *Fentzke and Janches*, 2008; *Janches et al.*, 2009]. The Rothera data and model provide a unique opportunity to further the understanding of the mesospheric metal layers at high latitudes and their relationships to temperature, gravity wave dynamics, meteoric input, and heterogeneous chemistry.

2. Observations

[7] The Fe lidar deployment at Rothera was a collaborative effort between the British Antarctic Survey and the University of Illinois at Urbana-Champaign. An overview of the Rothera campaign is reported by *Chu et al.* [2006]. The key instrument was the University of Illinois Fe Boltzmann temperature lidar that was previously deployed at the South Pole from November 1999 to October 2001 [*Chu et al.*, 2003; *Pan and Gardner*, 2003; *Gardner et al.*, 2005]. This lidar is capable of measuring temperatures using the Rayleigh technique from about 30 to 70 km [e.g., *Hauchecorne et al.*, 1991] and using the Fe Boltzmann technique from about 75 to 100 km [*Gelbwachs*, 1994]. It also measures Fe densities from 70 to 115 km, polar mesospheric clouds around 84 km, and polar stratospheric clouds near 20 km. An analysis of the lidar performance capabilities and their validation is in the work by *Chu et al.* [2002].

[8] Fe measurements were made during both day and night in all 12 months (see Table 1). About 545 hours of data taken on 69 different days are used in this study. The Fe densities were derived from simultaneous two-channel observations at 372 and 374 nm using the data processing procedures described by *Gardner et al.* [2005]. This approach enables Fe densities to be measured even in the presence of PMCs. Sporadic Fe layers (Fe_S) sometimes occur at high altitudes above 95 km during summer months (November–February). The contributions of Fe_S to the main Fe layer are negligible, but their influence at higher altitudes near 100 km can be significant. As reported by *Diettrich*

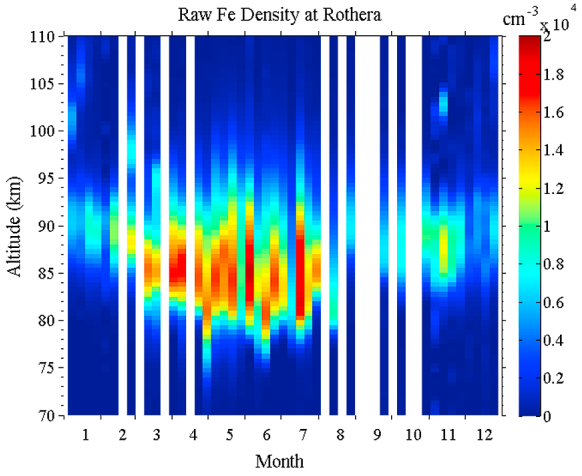

Figure 1. Weekly mean density profiles of the mesospheric Fe layers observed at Rothera, Antarctica; vertical resolution is 500 m.

et al. [2006], Fe_S are common at Rothera during summer (~18% occurrence probability), so we did not exclude them from the Fe data set presented here. The Fe layer abundance, centroid altitude, and RMS width were calculated using only the Fe density data below 100 km, which includes the main layer but excludes most Fe_S layers. Consequently, these fundamental parameters are largely free of Fe_S layer effects. Although the data were collected at a fundamental range resolution of 48 m, the Fe profiles were smoothed vertically with a 1 km full width at half maximum Hamming window to reveal the background structure of the layer. The weekly mean density profiles are plotted in contour format in Figure 1 at a vertical resolution of 500 m. The largest data gaps are 3 weeks in August–September and 2 weeks in October.

[9] To further characterize the seasonal variations, the weekly mean profiles shown in Figure 1 were interpolated over gaps in the observations and smoothed using the procedure employed by *Gardner et al.* [2005] to process the South Pole data. The technique eliminates temporal fluctuations with periods less than ~4 weeks and substantially reduces the amplitudes of fluctuations with periods of ~2 months or less. The resulting Fe density climatology is plotted in Figure 2a between 70 and 110 km at resolutions of 500 m and 1 week.

3. Seasonal Variations of the Fe Layer at Rothera as Observed by Lidar

3.1. Observational Results

[10] The Fe profiles exhibit substantial variations throughout the year. During austral summer, especially in December and January, Fe densities are very low and the layer is confined to a narrow range of altitudes between about 85 and 95 km. In February and March the layer exhibits significant growth, especially below 85 km, as it transitions to its high-density, autumn-winter state between about 75 and 100 km in April through mid-July. The maximum density ~16,000 cm^{-3} occurs in late April near 85 km altitude, more than 2 months earlier than at South Pole (see Figure 4b). Beginning in late July and August the Fe layer rapidly dissipates but experiences a modest rebound in the densities between 85 and 90 km during October and early November before transitioning to the high, thin, midsummer state. At the South Pole this secondary Fe maximum in late spring is far less prominent and occurs at a higher altitude (between 90 and 92 km, see Figure 4).

[11] The Fe layer column abundances, centroid altitudes, and RMS widths were derived from the weekly mean Fe density profiles displayed in Figure 1 and are plotted versus month in Figure 3. A harmonic fit consisting of mean plus annual and semiannual oscillations, equation (1), is applied to the data to further characterize their seasonal variations,

$$y = A_0 + A_{12}\cos\left[\frac{2\pi}{365}(\text{day} - P_{12})\right] + A_6\cos\left[\frac{2\pi}{365/2}(\text{day} - P_6)\right]. \quad (1)$$

The results are shown as solid curves in Figure 3 and the fitting parameters (A_0, A_6, A_{12}, P_6, and P_{12}) are summarized in Table 2. The Fe abundance, centroid altitude, and RMS width are all dominated by strong annual oscillations at Rothera, while semiannual oscillations are also apparent in the data. For comparison, the harmonic fits for the Fe observations at the South Pole (90°S) are plotted as dashed

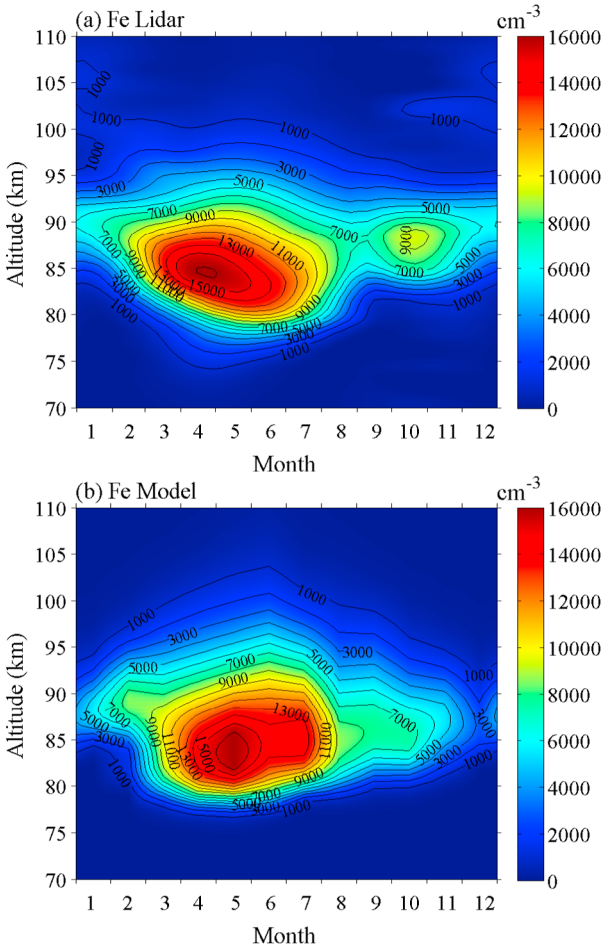

Figure 2. (a) Observed weekly mean Fe density climatology and (b) modeled Fe density climatology at Rothera, Antarctica.

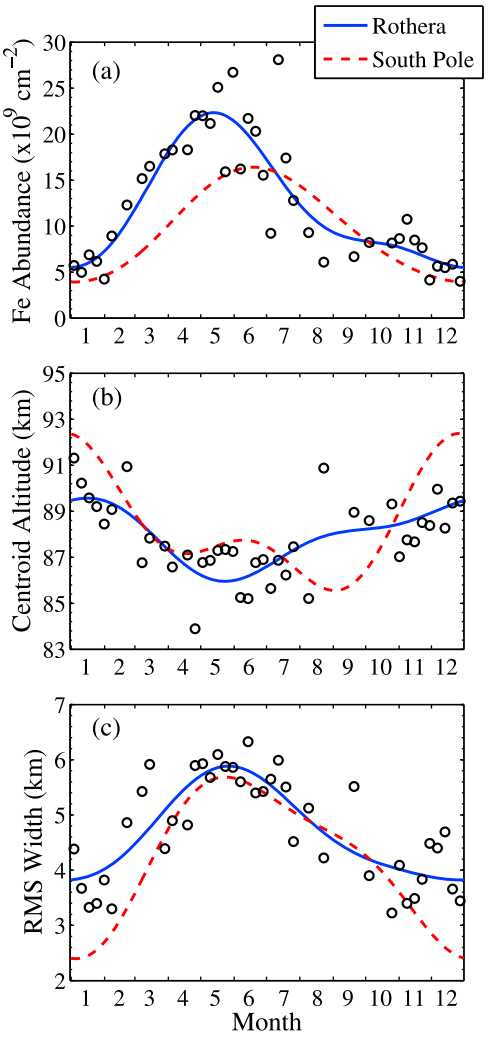

Figure 3. Seasonal variations of weekly mean Fe layer (a) column abundance, (b) centroid altitude, and (c) RMS width. Data points at Rothera are marked as circles, and the harmonic fits (mean + annual + semiannual) are plotted as solid and dashed curves for Rothera and the South Pole, respectively. The South Pole data were taken from *Gardner et al.* [2005].

curves in Figure 3. We also include in Table 2 the parameters of the South Pole harmonic models taken from *Gardner et al.* [2005].

[12] The weekly mean Fe abundance at Rothera varies from 4.0×10^9 to 28.1×10^9 cm^{-2} and the annual mean is 12.3×10^9 cm^{-2}, about 20% larger than the South Pole annual mean of 9.7×10^9 cm^{-2}. Such a difference is insignificant considering that lidar calibration errors could result in Fe density and abundance errors of ±10%. While the annual amplitudes at Rothera and the South Pole are comparable, the semiannual amplitude at Rothera is about 3 times larger than the South Pole value. The stronger semiannual amplitude at Rothera is associated with the main abundance maximum in early May and the secondary maximum in October–November (see Figures 1 and 2a). The annual oscillations peak in May (day 142), while the semiannual oscillations peak in late April (day 126) and early November (day 308). Both Rothera oscillations lead the corresponding South Pole oscillations by about 1 month.

[13] The Fe layer centroid altitude ranges from 83.9 to 91.3 km with a mean of 87.9 km. The annual mean centroid altitude is 0.5 km lower than that at the South Pole. At Rothera the seasonal variations of the centroid altitude are governed by a strong annual oscillation with the lowest heights occurring from April to July. The semiannual oscillation is weaker with an amplitude just 40% of the annual amplitude. In contrast at the South Pole, the annual and semiannual centroid oscillations are comparable in magnitude. The RMS width of the Fe layer ranges from 3.2 to 6.3 km with a mean of 4.7 km, which is considerably smaller than the range observed at South Pole (2.0–6.8 km, mean 4.2 km, RMS width average is 12% larger). The Rothera Fe layer is broader than the South Pole layer through most of the year with the biggest difference in summer (RMS width is 3.8 km at Rothera versus 2.4 km at the South Pole).

3.2. Relationships to PMC, Temperature, MIF, and Vertical Transport

3.2.1. Heterogeneous Removal of Fe Atoms by PMC Ice Particles

[14] *Plane et al.* [2004] have shown that the uptake of metallic species by water ice particles is highly efficient and can result in the complete removal of Fe inside a strong

Table 2. Parameters of Harmonic Models for Seasonal Variations in Measured Fe Layer Abundances, Centroid Altitudes, and RMS Widths at Rothera and the South Pole[a]

	Annual Mean A_0	Annual Amplitude A_{12}	Annual Phase P_{12}	Semiannual Amplitude A_6	Semiannual Phase P_6
			Abundance		
Rothera	12.3 ± 0.6	7.6 ± 0.7	142 ± 7	2.6 ± 0.8	126 ± 9
S. Pole	9.7 ± 0.8	6.2 ± 1.1	175 ± 10	0.6 ± 1.1	156 ± 51
			Centroid Altitude		
Rothera	87.9 ± 0.2	1.5 ± 0.2	347 ± 12	0.6 ± 0.3	39 ± 14
S. Pole	88.4 ± 0.2	2.5 ± 0.3	11 ± 7	1.6 ± 0.3	173 ± 5
			RMS Width		
Rothera	4.7 ± 0.1	1.0 ± 0.1	154 ± 8	0.2 ± 0.1	138 ± 21
S. Pole	4.2 ± 0.1	1.5 ± 0.1	173 ± 6	0.4 ± 0.1	111 ± 10

[a]From *Gardner et al.* [2005]. Means and amplitudes for abundances, centroid altitudes, and RMS widths are given as $\times 10^9$ cm^{-2}, km, and km, respectively; phases are in days.

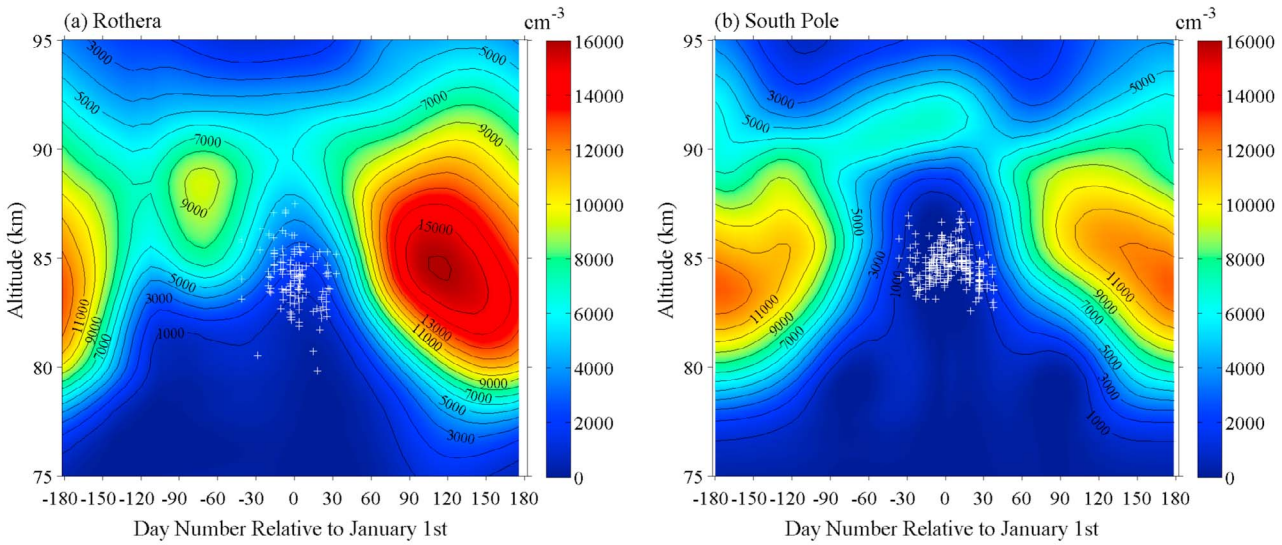

Figure 4. Fe density profiles and the summer PMC altitude distributions plotted versus altitude and day number for (a) Rothera and (b) the South Pole.

PMC layer. Lidar observations have provided compelling evidence for significant depletion of Fe, Na, and K in the presence of PMCs during the polar summer [*Plane et al.*, 2004; *Lübken and Höffner*, 2004; *Gardner et al.*, 2005; *Thayer and Pan*, 2006; *Raizada et al.*, 2007]. PMC brightness, occurrence frequency, and height range depend on temperature and vertical wind speeds, which vary strongly with latitude and season. *Chu et al.* [2003, 2006] have shown that the Rothera PMCs occur about 1 km lower, are observed about one third as frequently, and are about one third the brightness as the South Pole PMCs. These differences are reflected in differences in the metal layer abundances, heights, and widths during the summer season at the two sites.

[15] In Figure 4 we have plotted the Fe densities between 75 and 95 km versus day number relative to 1 January for both Rothera and the South Pole. Also plotted on the Fe contours (white crosses) are the PMCs observed at each site with the Fe lidar. The extensive and persistent PMC layers overlap the regions where Fe atoms are depleted at both sites. As modeled by *Plane et al.* [2004] and *Gardner et al.* [2005], such persistent and strong clouds provide sufficient ice volumetric surface areas to almost completely remove Fe atoms in their vicinity and push the peak of Fe layers to well above 90 km. The gap between the depletion ledges and the highest clouds suggest that there are additional ice particles, invisible to the lidar, which also play an important role in the heterogeneous removal of Fe atoms at both sites. These subvisible ice particles are detectable by radar as polar mesosphere summer echoes (PMSEs) when charges are attached and neutral air turbulence creates a gradient in electron density [*Rapp and Lübken*, 2004]. The mean PMSE heights are known to extend above PMC layers by as much as several kilometers [*Klekociuk et al.*, 2008; *Kirkwood et al.*, 2008; *Morris et al.*, 2009]. This effect of heterogeneous removal of Fe atoms by ice particles is more prominent and extensive at the South Pole where the colder temperatures are more favorable for ice particle formation and the depletion clearly extends several kilometers above the highest visible mesospheric clouds.

[16] To further illustrate the PMC effects on Fe profiles, we take a summer mean of Fe density profiles over ±31 days surrounding 1 January, and then overplot the PMC total backscatter coefficient, β_{Total}, with the summer Fe profiles in Figures 5a and 5b for Rothera and the South Pole, respectively. The PMCs at the South Pole are apparently

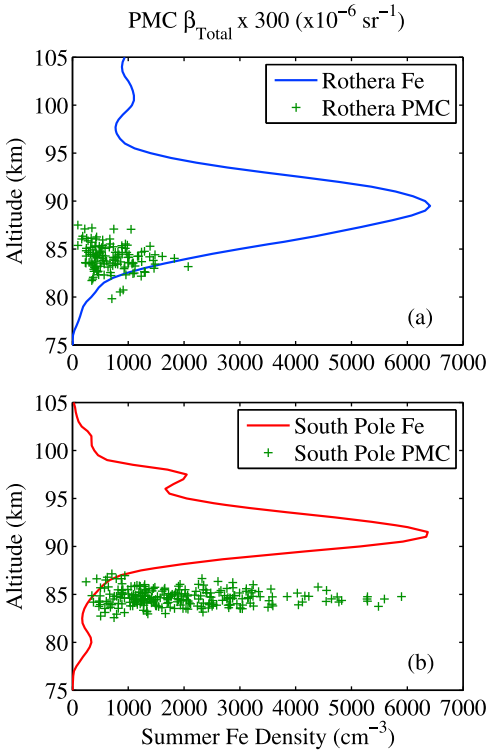

Figure 5. Summer Fe density profile averaged over ±31 days surrounding 1 January, overplotted with the PMC total backscatter coefficients β_{Total} for (a) Rothera and (b) the South Pole. Note that the values of β_{Total} have been multiplied by 300 in both plots.

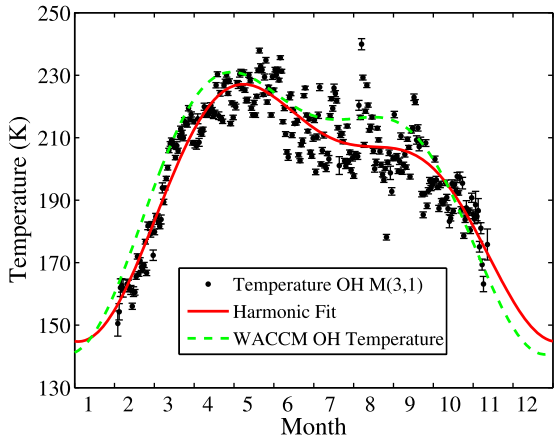

Figure 6. Time series of OH Meinel (3,1) band nightglow temperatures and their standard errors measured at Rothera during 2002–2005, the harmonic fit, and the WACCM modeled temperatures.

much brighter than at Rothera and a dip in the Fe density profile around the PMC altitudes is quite obvious from Figure 5b. Notice that the Fe densities within the visible cloud region at Rothera are considerably higher than at the South Pole. This is further evidence that both visible and subvisible ice particles are far less effective at depleting Fe at Rothera because the ice surface area is much smaller. Consistent with this interpretation, the summertime Rothera Fe layer is lower, wider, and has a larger abundance than the South Pole layer.

3.2.2. Dependence on Temperatures

[17] Fe abundances are also sensitive to the ambient temperature. Below 95 km, where most of the Fe resides at Rothera, Fe densities are highly correlated with temperature [e.g., *Gardner et al.*, 2005]. The reactions that convert the primary reservoir FeOH back to Fe have significant activation energies [*Plane et al.*, 2003; *Plane*, 2004], so the balance moves to atomic Fe at higher temperatures. This is further amplified because higher temperatures tend to shift the balance from O_3, which oxidizes Fe to its various reservoir species, toward atomic O and H which reduce compounds such as FeOH and FeO_3 back to Fe. Plotted in Figure 6 versus day number are the mesopause region temperatures inferred from the OH Meinel (3,1) vibrational-rotational band observed in the nightglow above Rothera using a Fourier-transform Michelson interferometer. The spectra were observed at solar zenith angles greater than 95°, and the line strengths of *Mies* [1974] were used to calculate the temperatures [*Espy et al.*, 2003]. On the basis of the observations of *Baker and Stair* [1988], the OH layer at Rothera is expected to peak near 87 km with a RMS width of ~3.7 km. Because the OH and Fe layers approximately overlap at Rothera, these temperatures can serve as a proxy for the thermal state of the whole Fe layer. After processing, the individual 5 min temperature values for each night were weighted with their fitting uncertainties and combined to form an average for that night that covered the period from 2002 to 2005, which includes the period when the lidar was present at Rothera. Each night's temperature and standard error of the mean that are presented in Figure 6 represent an average over all years that includes approximately 70 hours of observations during midwinter but falls to an average of approximately one hour near summer due to solar zenith angle restrictions. This averaging had the effect of smoothing out variations caused by short-period gravity waves as well as planetary waves, which are not coherent year to year. The harmonic fit parameters for the OH temperature time series are listed in Table 3.

[18] The temperature rises rapidly beginning in late summer, as adiabatic cooling associated with the meridional circulation system subsides, reaching the warmest values in late April and early May when the Fe abundance is also maximum. At midlatitudes in the Northern Hemisphere, where the temperature is too warm for PMCs to form, the measured temperature sensitivity of the Fe abundance is about 0.5×10^9 cm^{-2} K^{-1} [*Kane and Gardner*, 1993b]. Therefore, the ~30 K temperature increase from late February, after the PMC season, to late April appears to be responsible for most of the increase in Fe abundance during this period. Throughout the winter from early May to early September the temperature decreases slowly by about 10 K whereas the Fe abundance decreases by approximately 60% (~1.4×10^{10} cm^{-2}). While slowly falling temperatures are responsible for about one third (~5×10^9 cm^{-2}) of the wintertime decrease in Fe densities, other mechanisms play more prominent roles.

3.2.3. Role of Meteor Input Function (MIF)

[19] The meteor input flux of Fe depends on the mass distribution of meteoroids, their speed and orientation relative to the Earth's atmosphere, and the ablation physics [*Janches et al.*, 2006; *Vondrak et al.*, 2008]. These issues are discussed in more detail later (see section 4) but it is important to note that the MIF of Fe at Rothera varies seasonally by about a factor of two, with the highest input flux occurring in mid-March (flux = 9600 atom cm^{-2} s^{-1}), about 1 month before the Fe abundance is maximum (see Figure 7). The lowest MIF occurs in late winter (mid-September, flux = 4300 atom cm^{-2} s^{-1}) very near the same time the Fe densities reach a local minimum (see Figures 7 and 11). No doubt, the seasonal variation in the MIF plays an important role in the wintertime decrease in Fe densities.

3.2.4. Influence of Vertical Transport

[20] The speed with which the meteoric Fe is transported downward to chemical sinks below 85 km also plays a key role in shaping the Fe layer profile and its abundance. The

Table 3. Parameters of Harmonic Models for Seasonal Variations in OH Meinel (3,1) Band Nightglow Temperatures (T) Measured at Rothera, 2002–2005, and for WACCM Temperatures at the Peak of the OH Layer

	Annual Mean A_0 (K)	Annual Amplitude A_{12} (K)	Annual Phase P_{12} (days)	Semiannual Amplitude A_6 (K)	Semiannual Phase P_6 (days)
Observed OH T	192.7 ± 0.54	34.7 ± 0.89	172 ± 1	14.7 ± 0.78	102 ± 1
WACCM OH T	195.9 ± 1.3	39.1 ± 1.8	168 ± 3	16.8 ± 1.8	90 ± 3

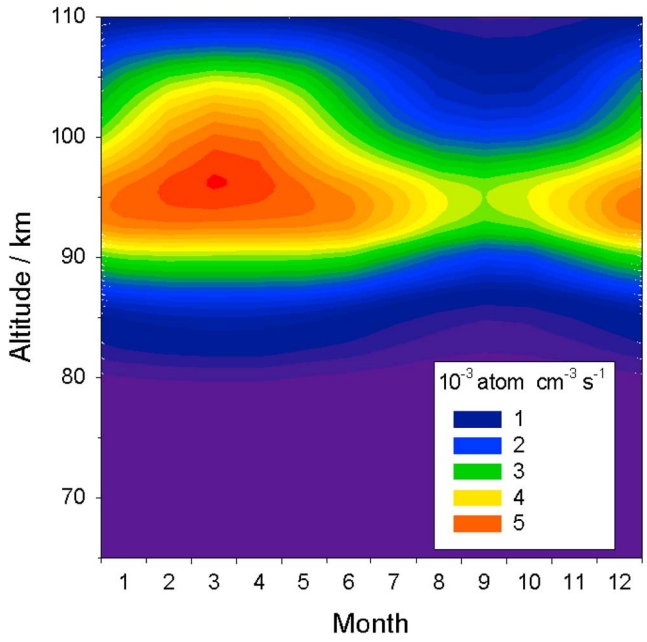

Figure 7. Seasonal variations of the Fe injection rate by meteoric ablation as a function of altitude and month.

dominant transport mechanisms in the mesopause region are associated with dissipating gravity waves. First, momentum deposition by the waves drives a meridional circulation that leads to significant vertical velocities at high latitudes during the solstices. Second, the dissipation of the waves leads to turbulent mixing. Gravity wave transport is characterized in most atmospheric models as a turbulent mixing process, which is modeled as a large-scale analog of molecular diffusion and parameterized using the eddy diffusion coefficient K_{zz} [e.g., *Chabrillat et al.*, 2002]. While the relationship between the gravity wave spectrum, the background atmospheric state, and K_{zz} is complex, in general stronger wave activity enhances turbulent mixing and the concomitant downward transport, which results in lower Fe densities.

[21] *Plane* [2004] has shown that the metal layer abundances are approximately inversely proportional to K_{zz}. Unfortunately, the precise value of K_{zz} and its seasonal variations are uncertain, in large part because the turbulence generated by breaking gravity waves is so difficult to measure. Gravity wave parameterization schemes have been developed to estimate K_{zz} by calculating how the waves are influenced by the background temperature and wind structure of the atmosphere through which they propagate [e.g., *Garcia and Solomon*, 1985]. *Yamashita et al.* [2009] characterized the seasonal variations of the gravity wave spectrum in the lower stratosphere (30–45 km) at Rothera using the atmospheric density profiles measured by the Fe lidar. They found that the majority (almost 60%) of the observed waves were propagating upward and the potential energy density of the wave spectrum varied annually with wintertime values averaging about 6 times larger than in summer. This is not surprising given that Rothera is located near high mountains along the Antarctic Peninsula at the edge of the wintertime polar vortex, both of which are known to be strong sources of gravity wave activity. While stratospheric waves are modified by the intervening wind and temperature fields as they propagate upward into the mesopause region [e.g., *Wang and Alexander*, 2009], in the absence of other observational data it is reasonable to assume that the seasonal variations of wave activity and K_{zz} are similar to those observed for the potential energy density in the stratosphere, namely small K_{zz} during the summer when major storms systems are relatively infrequent with much larger values in winter when the vortex is well established. In fact, *Espy et al.* [2006] reported that the wintertime gravity wave momentum flux was considerably larger at Rothera than at Halley Station, which is located well inland of the winter storm tracks.

[22] However, the generation and transmission of gravity waves in winter near the polar vortex is much more complicated than the scenario suggested by the *Yamashita et al.* [2009] stratospheric data set. The K_{zz} profiles employed in our modeling (see Figure 10b) were derived from a three-dimensional (3-D) global climate model using a detailed gravity wave parameterization scheme [*Garcia et al.*, 2007; *Marsh et al.*, 2007]. They exhibit large 4 month oscillations with the largest K_{zz} values in April, August, and December (which should lead to enhanced downward transport and lower Fe densities during these months) and the smallest values in mid-January to mid-February, July, and in September through November. The annual and semiannual oscillations of the predicted K_{zz} profiles are negligible. The implications are discussed further in section 4.

4. Modeling the Fe Layer at Rothera

[23] The structure of the Fe layer is governed by complex chemical and dynamical interactions among the MLT constituents and the meteoric influx of Fe. The seasonal variations in the Fe abundance are controlled predominantly by the seasonal changes in ambient temperature, MIF, vertical transport by gravity waves, and the heterogeneous uptake on ice and smoke particles. The seasonal variations in minor species such as O, H, and O_3 play a secondary role. In this paper we use the FeMOD model, which determines the major species Fe, FeOH, and Fe^+ by full solution of their respective continuity equations [*Gardner et al.*, 2005]. The other iron species (e.g., FeO, FeO_2, FeO_3, FeO^+) are short-lived intermediates considered to be in a chemical steady state. The gas phase reactions of iron and their rate coefficients are taken from *Plane et al.* [2003], *Vondrak et al.* [2006], and *Woodcock et al.* [2006]. FeMOD is one-dimensional (1-D), extending from 65 to 110 km with a height resolution of 0.5 km. The continuity equations are integrated with a 10 min time step using a time implicit integration scheme [*Shimazaki*, 1985].

[24] The input of atomic Fe due to meteoric activity was modeled by combining two models, a Chemical Ablation Model (CABMOD) [*Vondrak et al.*, 2008] with a model of the seasonal and geographical variability of the MIF, which is based on the astronomical origin of the meteoroids [*Janches et al.*, 2006; *Fentzke and Janches*, 2008]. Look-up tables of the individual ablation profiles predicted by CABMOD for eight metallic species (see examples in *Janches et al.* [2009]) were calculated as a function of meteoroid mass, velocity, and entry angle. The tables were calculated covering a 1×10^{-5} to 5×10^3 μg mass range, a 11–72 km s^{-1} velocity range, and a range of 0°–89° in entry angle [*Fentzke and Janches*, 2008]. The resolutions were three divisions per decade

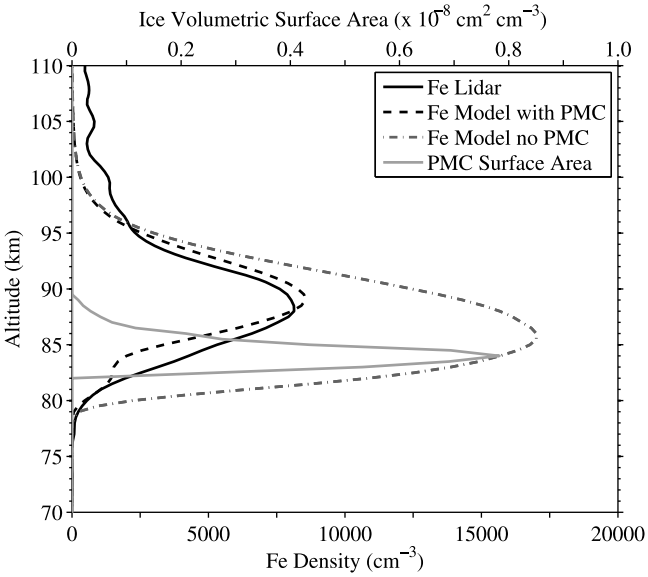

Figure 8. The Fe layer at Rothera in February. The modeled layer (solid black curve) compares well with the lidar observations (dashed black curve), when PMCs (volumetric surface area shown by the gray line; units on upper *x* axis) are included. If PMCs are not present, the modeled layer (dash-dotted gray curve) is too low with an abundance that is more than twice that observed.

$\log_{10}$(mass), 5 km s^{-1}, and 5° for the mass, velocity, and entry angle, respectively. The MIF model takes into account the instantaneous position, with respect to the local frame of reference, of the six main meteoroid apparent sources and uses Monte Carlo simulation to select the meteoroid properties. Once these are determined, an interpolation of the look-up tables is performed to determine the elemental ablation profiles as a function of altitude. These are then added for all cases counted in 24 hours. Figure 7 (and Figure 11) shows the seasonal Fe input rate at Rothera resulting from the combination of these models. This model sets the total mass flux at 10.0 t d^{-1}, as reported by *Ceplecha et al.* [1998].

[25] The concentrations of the minor constituents (O_3, O, H, H_2, H_2O, NO^+, O_2^+, and electrons) which control the Fe chemistry [*Plane*, 2003, Figure 15] are obtained from the National Center for Atmospheric Research (NCAR) Whole Atmosphere Chemistry Climate Model (WACCM) [*Garcia et al.*, 2007; *Marsh et al.*, 2007]. Here we use version 3.5.48 of WACCM which includes updates to gravity wave parameterization [*Richter et al.*, 2010] and to chemical kinetic reaction rates [*Sander et al.*, 2006]. Typically, WACCM is used as a free-running climate model, and will not reproduce the atmospheric conditions of any particular year. However, for this study, to better represent the conditions under which the observations at Rothera were taken, WACCM incorporated reanalysis data in the troposphere and stratosphere for 2004. This is achieved by relaxing the horizontal winds and temperatures to the version 5.2 reanalysis from the Goddard Earth Observing System Data Assimilation System (GEOS-5.2) [*Rienecker et al.*, 2008]. The relaxation to GEOS-5.2 occurs with a time scale of ~5 hours from the surface to 40 km. Between 40 and 50 km the amount of relaxation is linear reduced such that at 50 km the model is free-running. Figure 6 shows the temperature from WACCM at the height of the calculated maximum in the OH Meinel emission layer. The agreement between the magnitudes of the WACCM modeled temperatures and those inferred from the OH Meinel nightglow is good, as is the general seasonal behavior. However, the WACCM temperature climbs more rapidly in autumn and leads the OH temperature by about 2 weeks. Furthermore, the WACCM temperatures remain higher at midwinter, while the nightglow temperatures show a great deal of variability at midwinter and an overall lower average temperature there.

[26] The transport of the metal constituents is assumed to be governed by the same eddy diffusion coefficient (K_{zz}) up to the turbopause at about 100 km, and above this height by molecular diffusion. Coefficient K_{zz} was also taken from WACCM, but a scaling factor was introduced to allow for the lack of advective circulation in the 1-D model [*Holton*, 1986]. This was an adjustable parameter in the model. The best fit to the lidar observations of Fe was achieved when the WACCM K_{zz} was increased by a factor of 2.4. Of course, this factor is sensitive to the absolute value of the MIF [*Plane*, 2004].

[27] PMCs were turned on in the model when the temperatures fell below 150 K, that is, from November to February. We used the same vertical profile of PMC volumetric surface area as in *Gardner et al.* [2005], but with two differences based on a comparison of the lidar observations at Rothera and the South Pole [*Chu et al.*, 2003, 2006]. First, the PMC layer height was decreased by 2.5 km to peak at 84 km, in accord with the lidar observations (Figure 9), and the volumetric surface area was reduced by a fitted factor of 3.1 in December and February, which accords with the smaller backscatter ratio of the Rothera PMCs and their lower occurrence frequency of around 20% in these months [*Chu et al.*, 2006, Figure 2]. The reduction factor was only 1.5 in January, which reflects the approximate doubling in the PMC occurrence frequency and brightness. Figure 8 shows a satisfactory fit of the modeled Fe layer to the observations, but also shows that without PMCs the agreement is poor; the layer is too low and the Fe column abundance is more than double that observed. It is important to note that the version of WACCM employed for this study predicts a summer mesopause that is about 7 km lower than measured (e.g., by the SABER instrument on the TIMED satellite (A. Smith, NCAR, personal communication, 2010)). Therefore, if the WACCM temperature profile had been used to predict the height of the PMCs, the heights would have been too low with respect to the underside of the Fe layer. For this reason the PMCs in the 1-D model are placed at 84 km, based on the lidar observations.

[28] Figure 2b is a contour plot showing the modeled annual Fe layer. Comparison with Figure 2a shows generally good agreement in terms of the summertime minimum, the late autumn maximum, and the decline in the layer abundance from July to December. Figure 9 compares the layer abundances, centroid altitudes, and RMS widths that were derived from the density contours plotted in Figure 2 and fitted to a harmonic model given by equation (1); the harmonic fit parameters are tabulated in Table 4. Figure 9 shows that the model captures the broad features of the

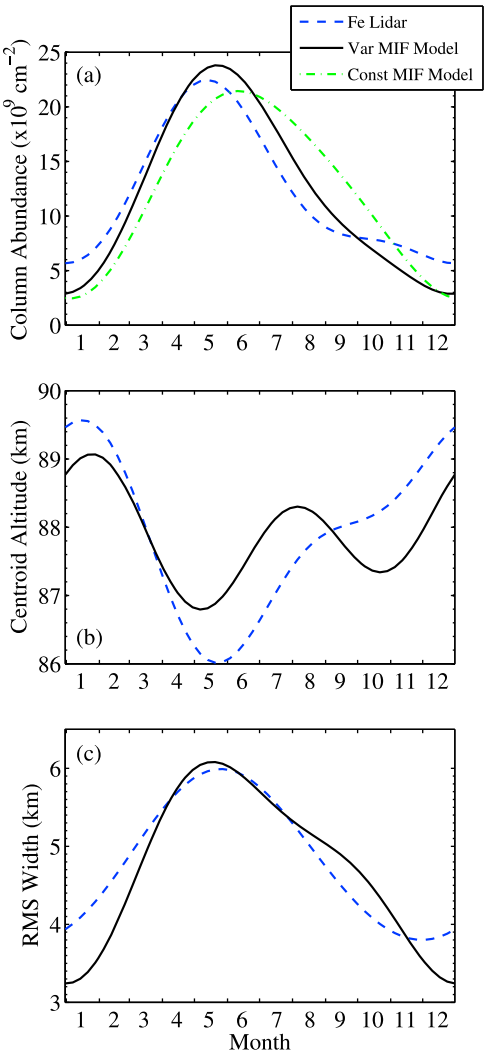

Figure 9. Comparison of modeled and observed column abundance, centroid altitude, and RMS width of the Fe layers at Rothera. All parameters were derived from the Fe climatologies shown in Figure 2 and then fitted to a harmonic model given in equation (1). Corresponding fitting parameters are in Table 4.

seasonal variations, particularly the abundance maximum in April–May. The observed abundance peaks in early May and then decreases throughout the winter. Note that if a constant MIF is used (Figure 9, dash-dotted green curve), then the modeled abundance exhibits a maximum that is 36 days later than observed, and the variations are symmetric around the solstice. This is good evidence for the importance of the MIF in determining the seasonal variations of Fe.

[29] Figure 10 illustrates the monthly variation predicted by WACCM of the minor species which control the Fe abundance (O_3, O, H, and H_2O), as well as K_{zz} and temperature T at an altitude of 87 km which is close to the average peak height of the Fe layer. This shows that several of these parameters should cause Fe to decrease in March–April, whereas Fe peaks at this time of year (Figure 9a). These parameters include the following: (1) the large increase in K_{zz} in autumn, which should transport Fe more rapidly below the layer; (2) increasing O_3, which oxidizes Fe to various oxides and hydroxides; and (3) decreasing O and H, which reduce the Fe compounds such as FeO_3 and FeOH back to Fe. The parameters which increase Fe are as follows: (1) the warmest temperatures, which speed up the reactions with activation energies which convert Fe compounds to Fe, and (2) less importantly, decreasing H_2O, which converts Fe oxides to the more stable hydroxides [*Plane et al.*, 2003]. Clearly the combination of higher temperatures (Figure 6) and the peak in the MIF in March–April (Figure 7) more than offset the effects of the increasing K_{zz} and O_3, and of decreasing O and H. While the observations show a local minimum in Fe densities in mid-September that corresponds to the deep annual minimum in MIF (see Figure 7), the September minimum is not as distinct in the modeled Fe layer, which is most likely related to our assumptions regarding vertical transport during this time of the year.

[30] In Figure 11 the monthly relative meteoric input function from the present study for Rothera is compared with that used in our previous study of the South Pole [*Gardner et al.*, 2005]. In the South Pole case, the MIF variation was taken from a radio meteor survey of sporadic meteors in the Northern Hemisphere [*Yrjola and Jenniskens*, 1998], to which a phase difference of 6 months has been

Table 4. Parameters of Harmonic Models for Seasonal Variations in Measured and Modeled Fe Layer Abundances, Centroid Altitudes, and RMS Widths Derived From Data in Figure 2[a]

	Annual Mean A_0	Annual Amplitude A_{12}	Annual Phase P_{12}	Semiannual Amplitude A_6	Semiannual Phase P_6
		Abundance			
Observed	12.3 ± 0.26	7.7 ± 0.36	140 ± 3	2.6 ± 0.36	127 ± 4
Variable MIF model	12.2 ± 0.29	9.9 ± 0.39	154 ± 2	2.1 ± 0.41	129 ± 5
Constant MIF model	12.3 ± 0.35	9.3 ± 0.47	176 ± 3	1.1 ± 0.49	121 ± 12
		Centroid Altitude			
Observed	87.9 ± 0.15	1.46 ± 0.22	349 ± 9	0.59 ± 0.22	36 ± 11
Variable MIF model	87.9 ± 0.15	0.47 ± 0.20	359 ± 27	0.79 ± 0.21	30 ± 8
		RMS Width			
Observed	4.86 ± 0.11	1.09 ± 0.16	148 ± 9	0.05 ± 0.16	129 ± 98
Variable MIF model	4.76 ± 0.07	1.28 ± 0.09	166 ± 5	0.36 ± 0.09	109 ± 8

[a]Means and amplitudes for abundances, centroid altitudes, and RMS widths are given as $\times 10^9$ cm^{-2}, km, and km, respectively; phases are in days.

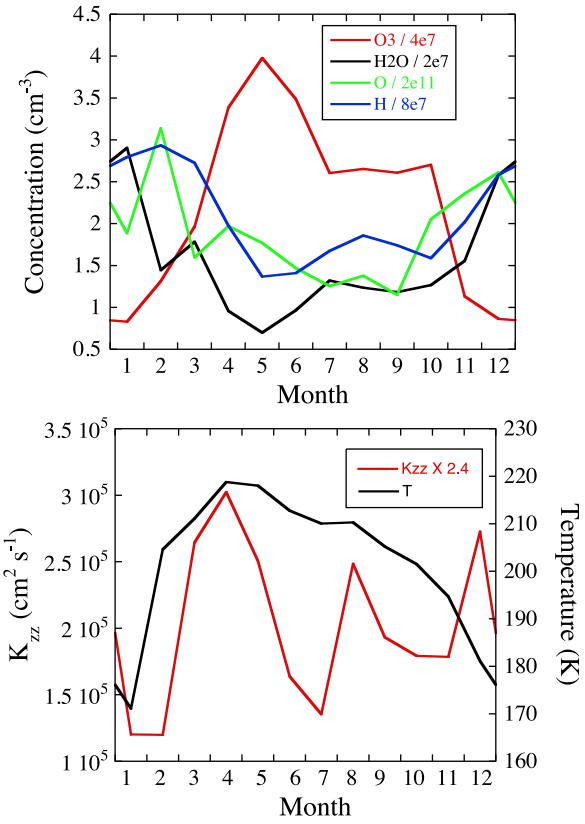

Figure 10. Monthly variations at 87 km in (top) O_3, H_2O, O, and H and (bottom) K_{zz} and temperature, as predicted by WACCM for 2004 at Rothera.

applied. While the MIF model used in the current study includes important improvements, the seasonal variations at Rothera and the South Pole are similar in both magnitude and phase. Although there is some evidence in the South Pole lidar data for Na [*Gardner et al.*, 2005], and to a lesser extent for Fe, peaking in the late autumn when the MIF is maximum rather than in midwinter, the autumnal maximum is much less pronounced at the South Pole. The reasons are that the seasonal variations of the Na and Fe densities at the South Pole are dominated by temperature and meridional convergence, which mask the effects of the MIF.

[31] Figures 9b and 9c compare the modeled and observed layer centroid altitudes and RMS widths. The modeled and observed RMS widths are in good agreement while the modeled centroid altitudes are too low in summer by about 0.5 km and too high in winter by about 1 km. In fact, the annual amplitude of the modeled centroid altitude (0.47 ± 0.20 km) is only one third of the value of the observed amplitude (1.46 ± 0.22 km). Agreement is reasonable in summer, when the layer is narrow and relatively high. In winter the model predicts slightly too much Fe on the topside, so that the centroid altitude is higher than the observations. This is also clear from comparing the contour plots in Figure 2. The reason is that iron is being partitioned into Fe rather than Fe^+ above 90 km. One possible explanation is that the atomic O in the model is too low between 90 and 105 km during winter. The role of atomic O is to destroy molecular ions such as FeO^+ ($FeO^+ + O \rightarrow Fe^+ + O_2$), which would otherwise undergo dissociative electron recombination to form Fe [*Woodcock et al.*, 2006]. For example, doubling the atomic O profile during June brings the modeled and measured centroid altitudes into good agreement.

[32] The differences between the observed and modeled means and semiannual amplitudes of the centroid altitudes are not significant (agreeing to within one standard deviation). There does appear to be a significant discrepancy in the amplitudes of the annual components, which could be related to errors in modeling vertical transport of Fe using only eddy transport in a 1-D model. However, the phases of the observed and modeled annual oscillations are 349 and 359 days, respectively, in agreement within the fitting errors. These correspond to a maximum in the annual variation around mid to late December, which is the time of maximum upwelling associated with the meridional circulation system. The small annual amplitude derived from the modeled centroid altitude oscillations suggests that the vertical transport in the 1-D model does not capture winter/summer circulation adequately. It is hoped that future modeling efforts using a fully consistent 3-D model will address this deficiency.

5. Conclusions

[33] The observed seasonal variations of Fe layer are considerably different at Rothera compared to the South Pole. Our current modeling efforts, which include an improved model for the meteor input function, appear to account for most of the key features of these high-latitude observations. The seasonal variations in the Fe abundance are controlled predominantly by the seasonal changes in ambient temperature, MIF, vertical transport by gravity waves, and the heterogeneous uptake on ice and smoke particles. These factors dominate the smaller variations of Fe arising from changes in minor constituents such as O, H, and O_3. During summer at both sites, cold temperatures coupled with the uptake of Fe atoms by PMC ice particles lead to minimum layer abundances in December and January. However, Fe depletion by these ice particles below 88 km is less effective at Rothera than at the South Pole because the Rothera PMCs are weaker, less extensive, and they occur at lower altitudes [*Chu et al.*, 2006]. Fe densities within the visible PMC

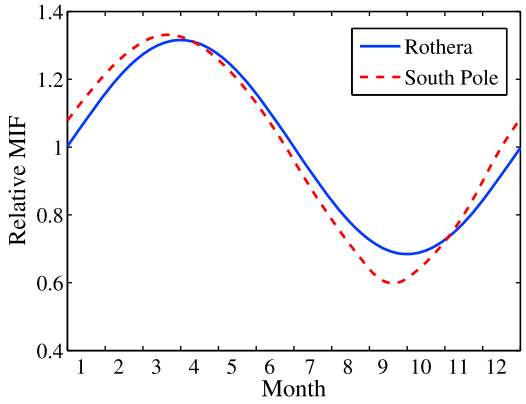

Figure 11. Comparison of the relative meteor input flux (MIF) functions used in the modeling of Rothera and South Pole Fe layers.

region are partially depleted at Rothera, while at the South Pole bright PMCs have been observed to remove all the Fe in their vicinity. As a result, the Fe layer is more than 3 km lower at Rothera in midsummer compared to the South Pole, and Rothera Fe densities within the PMC region are considerably larger than at the South Pole.

[34] At Rothera the Fe abundance variations in early autumn through late spring are driven primarily by temperature and MIF. All three parameters peak in the late autumn (early May) and then decline throughout the winter. At the South Pole the Fe abundance variations, which are approximately symmetrical about a midwinter peak in early June, are driven primarily by temperature and meridional flux convergence, which are also maximum in midwinter and dominate the smaller impact of MIF.

[35] The absolute annual average Fe injection rate in the present Rothera model is 7.2×10^3 atoms cm^{-2} s^{-1}, which is nearly a factor of 5 times smaller than the average injection rate of 3.4×10^4 atoms cm^{-2} s^{-1} that gave the best fit of the South Pole model to the observations. This difference arises because the average K_{zz} values between 80 and 90 km in WACCM, even after being increased by a factor of 2.4 (see above), are still a factor of 4.1 times smaller (averaged over the year), than the average K_{zz} values from the two-dimensional SOCRATES model [*Chabrillat et al.*, 2002] that we used previously. This comparison once again demonstrates the sensitivity of the metal atom densities to the balance between injection by meteoric ablation and the removal by downward vertical transport. In the future, direct measurements of the vertical flux of metal atoms using Na and Fe Doppler wind and temperature lidars should help resolve these two highly uncertain terms [*Gardner and Liu*, 2010].

[36] **Acknowledgments.** We gratefully acknowledge the lidar winter-over scientist Graeme J. Nott, the lidar engineer Jan C. Diettrich, and the staff of the British Antarctic Survey for their operational support of the Fe lidar and other correlative instruments at Rothera. The authors wish to thank Jonathan T. Fentzke for discussion on the MIF model. The Rothera lidar project was supported by the U. K. Natural Environmental Research Council and the U.S. National Science Foundation (NSF) grant ATM-0602334. X.C. and C.S.G. were partially supported by NSF grants ATM-0645584 and ANT-0839091. D.J. was supported under NSF grants ATM-05311464 and ATM-0525655 to Northwest Research Associates and agreement 51861-8406 between Cornell University and NWRA. The National Center for Atmospheric Research is sponsored by the National Science Foundation.

References

Alpers, M., J. Höffner, and U. von Zahn (1990), Iron atom densities in the polar mesosphere from lidar observations, *Geophys. Res. Lett.*, *17*, 2345–2348.

Baker, D. J., and A. T. Stair Jr. (1988), Rocket measurements of the altitude distributions of the hydroxyl airglow, *Phys. Scr.*, *37*, 611–622.

Bowman, M. R., A. J. Gibson, and M. C. W. Sandford (1969), Atmospheric sodium measured by a tuned laser radar, *Nature*, *221*, 456–457.

Ceplecha, Z., J. Borovicka, W. G. Elford, D. O. Revelle, R. L. Hawkes, V. Porubcan, and M. Simek (1998), Meteor phenomena and bodies, *Space Sci. Rev.*, *84*, 327–471.

Chabrillat, S., G. Kockarts, D. Fonteyn, and G. Brasseur (2002), Impact of molecular diffusion on the CO_2 distribution and temperature in the mesosphere, *Geophys. Res. Lett.*, *29*(15), 1729, doi:10.1029/2002GL015309.

Chu, X., and G. Papen (2005), Resonance fluorescence lidar for measurements of the middle and upper atmosphere, in *Laser Remote Sensing*, edited by T. Fujii and T. Fukuchi, pp. 179–432, CRC Press, Boca Raton, Fla.

Chu, X., G. Papen, W. Pan, C. S. Gardner, and J. Gelbwachs (2002), Fe Boltzmann temperature lidar: Design, error analysis, and first results from the North and South poles, *Appl. Opt.*, *41*, 4400–4410.

Chu, X., C. S. Gardner, and R. G. Roble (2003), Lidar studies of interannual, seasonal, and diurnal variations of polar mesospheric clouds at the South Pole, *J. Geophys. Res.*, *108*(D8), 8447, doi:10.1029/2002JD002524.

Chu, X., G. J. Nott, P. J. Espy, C. S. Gardner, J. C. Diettrich, M. A. Clilverd, and M. J. Jarvis (2004), Lidar observations of polar mesospheric clouds at Rothera, Antarctica (67.5°S, 68.0°W), *Geophys. Res. Lett.*, *31*, L02114, doi:10.1029/2003GL018638.

Chu, X., P. J. Espy, G. J. Nott, J. C. Diettrich, and C. S. Gardner (2006), Polar mesospheric clouds observed by an iron Boltzmann lidar at Rothera (67.5°S, 68.0°W), Antarctica from 2002 to 2005: Properties and implications, *J. Geophys. Res.*, *111*, D20213, doi:10.1029/2006JD007086.

Diettrich, J. C., G. J. Nott, P. J. Espy, X. Chu, and D. Riggin (2006), Statistics of sporadic iron layers and relation to atmospheric dynamics, *J. Atmos. Sol. Terr. Phys.*, *68*, 101–113.

Espy, P. J., R. E. Hibbins, G. O. L. Jones, D. M. Riggin, and D. C. Fritts (2003), Rapid, large-scale temperature changes in the polar mesosphere and their relationship to meridional flows, *Geophys. Res. Lett.*, *30*(5), 1240, doi:10.1029/2002GL016452.

Espy, P. J., R. E. Hibbins, G. R. Swenson, J. Tang, M. J. Taylor, D. M. Riggin, and D. C. Fritts (2006), Regional variations of mesospheric gravity wave momentum flux over Antarctica, *Ann. Geophys.*, *24*, 81–88.

Felix, F., W. Keenliside, G. Kent, and M. C. W. Sandford (1973), Laser radar observations of atmospheric potassium, *Nature*, *246*, 345–346, doi:10.1038/246345a0.

Fentzke, J. T., and D. Janches (2008), A semiempirical model of the contribution from sporadic meteoroid sources on the meteor input function observed at Arecibo, *J. Geophys. Res.*, *113*, A03304, doi:10.1029/2007JA012531.

Garcia, R. R., and S. Solomon (1985), The effect of breaking gravity waves on the dynamics and chemical composition of the mesosphere and lower thermosphere, *J. Atmos. Sci.*, *90*, 3850–3868.

Garcia, R. R., D. R. Marsh, D. E. Kinnison, B. A. Boville, and F. Sassi (2007), Simulations of secular trends in the middle atmosphere, 1950–2003, *J. Geophys. Res.*, *112*, D09301, doi:10.1029/2006JD007485.

Gardner, C. S., and A. Z. Liu (2010), Wave-induced transport of atmospheric constituents and its effect on the mesospheric Na layer, *J. Geophys. Res.*, *115*, D20302, doi:10.1029/2010JD014140.

Gardner, C. S., G. C. Papen, X. Chu, and W. Pan (2001), First lidar observations of middle atmosphere temperatures, Fe densities, and polar mesospheric clouds over the north and south poles, *Geophys. Res. Lett.*, *28*, 1199–1202, doi:10.1029/2000GL012622.

Gardner, C. S., J. M. C. Plane, W. Pan, T. Vondrak, B. J. Murray, and X. Chu (2005), Seasonal variations of the Na and Fe layers at the South Pole and their implications for the chemistry and general circulation of the polar mesosphere, *J. Geophys. Res.*, *110*, D10302, doi:10.1029/2004JD005670.

Gelbwachs, J. A. (1994), Iron Boltzmann factor lidar: Proposed new remote sensing technique for mesospheric temperature, *Appl. Opt.*, *33*, 7151–7156.

Gerding, M., M. Alpers, U. von Zahn, R. J. Rollason, and J. M. C. Plane (2000), Atmospheric Ca and Ca+ layers: Midlatitude observations and modeling, *J. Geophys. Res.*, *105*, 27,131–27,146.

Granier, C., J. P. Jegou, and G. Megie (1985), Resonant lidar detection of Ca and Ca^+ in the upper atmosphere, *Geophys. Res. Lett.*, *12*, 655–658.

Granier, C., J. P. Jegou, and G. Megie (1989), Iron atoms and metallic species in the Earth's upper atmosphere, *Geophys. Res. Lett.*, *16*, 243–246.

Hauchecorne, A., M. L. Chanin, and P. Keckhut (1991), Climatology and trends of middle atmosphere temperatures (33–87 km) as seen by Rayleigh lidar over the south of France, *J. Geophys. Res.*, *96*, 15,297–15,309.

Helmer, M., J. M. C. Plane, J. Qian, and C. S. Gardner (1998), A model of meteoric iron in the upper atmosphere, *J. Geophys. Res.*, *103*, 10,913–10,925.

Holton, J. R. (1986), A dynamically based transport parameterization for one-dimensional photochemical models of the stratosphere, *J. Geophys. Res.*, *91*, 2681–2686.

Hunten, D. M. (1967), Spectroscopic studies of the twilight airglow, *Space Sci. Rev.*, *6*, 493–573.

Janches, D., C. J. Heinselman, J. L. Chau, A. Chandran, and R. Woodman (2006), Modeling the global micrometeor input function in the upper atmosphere observed by high power and large aperture radars, *J. Geophys. Res.*, *111*, A07317, doi:10.1029/2006JA011628.

Janches, D., L. P. Dyrud, S. L. Broadley, and J. M. C. Plane (2009), First observation of micrometeoroid differential ablation in the atmosphere, *Geophys. Res. Lett.*, *36*, L06101, doi:10.1029/2009GL037389.

Kane, T. J., and C. S. Gardner (1993a), Lidar observations of the meteoric deposition of mesospheric metals, *Science*, *259*, 1297–1300.

Kane, T. J., and C. S. Gardner (1993b), Structure and seasonal variability of the nighttime mesospheric Fe layer at midlatitudes, *J. Geophys. Res.*, *98*, 16,875–16,886.

Kirkwood, S., H. Nilsson, R. J. Morris, A. R. Klekociuk, D. A. Holdsworth, and N. J. Mitchell (2008), A new height for the summer mesopause: Antarctica, December 2007, *Geophys. Res. Lett.*, *35*, L23810, doi:10.1029/2008GL035915.

Klekociuk, A. R., R. J. Morris, and J. L. Innis (2008), First Southern Hemisphere common-volume measurements of PMC and PMSE, *Geophys. Res. Lett.*, *35*, L24804, doi:10.1029/2008GL035988.

Lübken, F. J., and J. Höffner (2004), Experimental evidence for ice particle interaction with metal atoms at the high latitude summer mesopause region, *Geophys. Res. Lett.*, *31*, L08103, doi:10.1029/2004GL019586.

Marsh, D. R., R. R. Garcia, D. E. Kinnison, B. A. Boville, F. Sassi, S. C. Solomon, and K. Matthes (2007), Modeling the whole atmosphere response to solar cycle changes in radiative and geomagnetic forcing, *J. Geophys. Res.*, *112*, D23306, doi:10.1029/2006JD008306.

Mies, F. H. (1974), Calculated vibrational transition probabilities of OH ($X^2\Pi$), *J. Mol. Spectrosc.*, *53*, 150–188.

Morris, R. J., A. R. Klekociuk, R. Latteck, W. Singer, D. A. Holdsworth, and D. J. Murphy (2009), Interhemispheric asymmetry in polar mesosphere summer echoes and temperature at 69° latitude, *J. Atmos. Sol. Terr. Phys.*, *71*, 464–469, doi:10.1016/j.jastp.2008.09.042.

Pan, W., and C. S. Gardner (2003), Seasonal variations of the atmospheric temperature structure at South Pole, *J. Geophys. Res.*, *108*(D18), 4564, doi:10.1029/2002JD003217.

Plane, J. M. C. (1991), The chemistry of meteoric metals in the Earth's upper atmosphere, *Int. Rev. Phys. Chem.*, *10*, 55–106.

Plane, J. M. C. (2003), Atmospheric chemistry of meteoric metals, *Chem. Rev.*, *103*, 4963–4984.

Plane, J. M. C. (2004), A time-resolved model of the mesospheric Na layer: Constraints on the meteor input function, *Atmos. Chem. Phys. Discuss.*, *4*, 39–69.

Plane, J. M. C., R. M. Cox, and R. J. Rollason (1999), Metallic layers in the mesopause and low thermosphere region, *Adv. Space Res.*, *24*, 1559–1570.

Plane, J. M. C., D. E. Self, T. Vondrak, and K. R. I. Woodcock (2003), Laboratory studies and modeling of mesospheric iron chemistry, *Adv. Space Res.*, *32*, 699–708.

Plane, J. M. C., B. J. Murray, X. Z. Chu, and C. S. Gardner (2004), Removal of meteoric iron on polar mesospheric clouds, *Science*, *304*, 426–428.

Raizada, S., and C. A. Tepley (2003), Seasonal variation of mesospheric iron layers at Arecibo: First results from low-latitudes, *Geophys. Res. Lett.*, *30*(2), 1082, doi:10.1029/2002GL016537.

Raizada, S., M. Rapp, F.-J. Lübken, J. Höffner, M. Zecha, and J. M. C. Plane (2007), Effect of ice particles on the mesospheric potassium layer at Spitsbergen (78°N), *J. Geophys. Res.*, *112*, D08307, doi:10.1029/2005JD006938.

Rapp, M., and F.-J. Lübken (2004), Polar mesosphere summer echoes (PMSE): Review of observations and current understanding, *Atmos. Chem. Phys.*, *4*, 2601–2633.

Richter, J. H., F. Sassi, and R. R. Garcia (2010), Toward a physically based gravity wave source parameterization in a General Circulation Model, *J. Atmos. Sci.*, *67*, 136–156, doi:10.1175/2009JAS3112.1.

Rienecker, M. M., et al. (2008), The GEOS-5 Data Assimilation System: Documentation of versions 5.0.1, 5.1.0, and 5.2.0, *NASA Tech. Rep. Ser. Global Model. Data Assimilation*, *TM-2008-104606*, vol. 27, 118 pp.

Sander, S. P., et al. (2006), Chemical kinetics and photochemical data for use in atmospheric studies, *Evaluation 15*, *Publ. 06-2*, 523 pp., Jet Propul. Lab., Pasadena, Calif.

Saunders, R. W., and J. M. C. Plane (2006), A laboratory study of meteor smoke analogues: Composition, optical properties, and growth kinetics, *J. Atmos. Sol. Terr. Phys.*, *68*, 2182–2202.

Shimazaki, T. (1985), *Minor Constituents in the Middle Atmosphere*, Kluwer Acad., Dordrecht, Neth.

Slipher, V. M. (1929), Emission in the spectrum of light in the night sky, *Publ. Astron. Soc. Pac.*, *41*, 262–263.

Thayer, J. P., and W. Pan (2006), Lidar observations of sodium density depletions in the presence of polar mesospheric clouds, *J. Atmos. Sol. Terr. Phys.*, *68*, 85–92.

Vondrak, T., K. R. Woodcock, and J. M. C. Plane (2006), A kinetic study of the reactions of Fe^+ with N_2O, N_2, O_2, CO_2 and H_2O, and the ligand-switching reactions $Fe^+.X + Y \rightarrow Fe^+.Y + X$ ($X = N_2$, O_2, CO_2; $Y = O_2$, H_2O), *Phys. Chem. Chem. Phys.*, *8*, 503–512.

Vondrak, T., J. M. C. Plane, S. L. Broadley, and D. Janches (2008), A chemical model of meteoric ablation, *Atmos. Chem. Phys.*, *8*, 7015–7031.

von Zahn, U., J. Höffner, and W. J. McNeil (2002), Meteor trails as observed by lidar, in *Meteors in the Earth's Atmosphere*, edited by E. Murad and I. P. Williams, pp. 149–187, Cambridge Univ. Press, Cambridge, U. K.

Wang, L., and J. Alexander (2009), Gravity wave activity during stratospheric sudden warmings in 2007–2008 Northern Hemisphere winter, *J. Geophys. Res.*, *114*, D18108, doi:10.1029/2009JD011867.

Woodcock, K. R. S., T. Vondrak, S. R. Meech, and J. M. C. Plane (2006), A kinetic study of the reactions $FeO^+ + O$, $Fe^+.N_2 + O$, $Fe^+.O_2 + O$ and $FeO^+ + CO$: Implications for sporadic E layers in the upper atmosphere, *Phys. Chem. Chem. Phys.*, *8*, 1812–1821.

Yamashita, C., X. Chu, H.-L. Liu, P. J. Espy, G. J. Nott, and W. Huang (2009), Stratospheric gravity wave characteristics and seasonal variations observed by lidar at the South Pole and Rothera, Antarctica, *J. Geophys. Res.*, *114*, D12101, doi:10.1029/2008JD011472.

Yi, F., C. Yu, S. Zhang, X. Yue, Y. He, C. Huang, Y. Zhang, and K. Huang (2009), Seasonal variations of the nocturnal mesospheric Na and Fe layers at 30°N, *J. Geophys. Res.*, *114*, D01301, doi:10.1029/2008JD010344.

Yrjola, I., and P. Jenniskens (1998), Meteor stream activity: VI, A survey of annual meteor activity by means of forward meteor scattering, *Astron. Astrophys.*, *330*, 739–752.

Zhou, Q., S. Raizada, C. A. Tepley, and J. M. C. Plane (2008), Seasonal and diurnal variation of electron and iron concentrations at the meteor heights above Arecibo, *J. Atmos. Sol. Terr. Phys.*, *70*, 49–60, doi:10.1016/j.jastp.2007.09.012.

X. Chu, Cooperative Institute for Research in Environmental Sciences, University of Colorado at Boulder, 216 UCB, Boulder, CO 80309, USA. (xinzhao.chu@colorado.edu)

P. J. Espy, Department of Physics, Norwegian University of Science and Technology, Trondheim N-7491, Norway.

C. S. Gardner, Department of Electrical and Computer Engineering, University of Illinois at Urbana-Champaign, 313 CSL Building, 1308 West Main Street, Urbana, IL 61801, USA.

D. Janches, Colorado Research Associates, Northwest Research Associates Inc., Boulder, CO 80301, USA.

D. R. Marsh, National Center for Atmospheric Research, PO Box 3000, Boulder, CO 80307, USA.

J. M. C. Plane, School of Chemistry, University of Leeds, Leeds LS2 9JT, UK.